TAMPEREEN TEKNILLINEN YLIOPISTO
TAMPERE UNIVERSITY OF TECHNOLOGY

AASHISH SAH

HIERARCHICAL NANOPATTERNING WITH BLOCK COPOLYMER LITHOGRAPHY AND TEMPLATE-STRIPPING

Bachelor of Science thesis

Examiner: Assoc. Prof. Tapio Niemi
Examiner and topic approved by the
Department of Natural Sciences
on 1st June 2018

ABSTRACT

AASHISH SAH: Hierarchical nanopatterning with block copolymer lithography and template-stripping
Tampere University of Technology
Bachelor of Science thesis, 31 pages
June 2018
International Bachelor's Degree Programme in Science & Technology
Major: Physics
Examiner: Assoc. Prof. Tapio Niemi
Keywords: block copolymers, directed self-assembly, photolithography, nano-imprint lithography, surface plasmon resonance, localized plasmon resonance, finite-difference time domain solver

The interest in confining light within the sub-wavelength regime has been motivated by the urgency in replacing electronic integrated circuits with optical ones for elevated computational efficiency. This can be achieved by using light as the signal-carrier instead of electrons. Like electrons, light needs circuits and components for the guidance of the signal. Consequently, the field of plasmonics studies the propagation, localization, and guidance of light in metal nanostructures (NSs) and metal thin films.

The hybridization of surface plasmon resonance (SPR) in periodic structures and localized surface plasmon resonance (LSPR) in metal NSs for light confinement and subsequent localization/enhancement is studied in this thesis. Fabrication of SPR inducing metal structures with feature sizes of 2 microns and 400 nm is achieved by photo- and nano-imprint lithography, respectively. LSPR inducing metal NSs with diameter between 45-55 nm and periodicity of 75 nm are realized by template-stripping of 150 nm thin Au film from silicon (Si) templates that were prepared by utilizing novel block copolymer (BCP) lithography.

Optical measurement and numerical modeling showed strong absorption of light at the wavelength of 687 nm for periodic Au nanodisks and at 708 nm for periodic Au nanodisks with metal NSs by BCP lithography, providing support for the existence of SPR and LSPR. However, BCP metal NSs without periodic Au nanodisks showed no plasmon resonance but exhibited an absorption of $\approx 20\%$ for wavelength range 350-800 nm. The efficacy of BCP directed self-assembly (DSA) for large-area hierarchical nanopatterning over other patterning schemes promises appealing prospect for sub-wavelength hierarchical nanopatterning.

ACKNOWLEDGEMENTS

I would like to express my gratitude to Prof. Tapio Niemi for providing me an opportunity to work in the Nanophotonics group despite my inadequate knowledge on this fascinating field of Nanophotonics. I would not have acquired the profound knowledge and invaluable experience in this field without his continuous guidance and unreserved support. I am eternally thankful to him for his unwavering endurance towards my repeated questionnaires throughout this thesis work.

I would like to convey my sincere thanks to Dr. Sozaraj Rasappa and Hanna Hulkkonen for explaining me just about everything despite their long hours in the cleanroom and also for letting me knock on their office doors at all times. I will always hold their mentoring with a great appreciation. Special thanks to Hanna for her insightful feedback on my thesis. Without the invaluable expertise from the members of this group, my research work in the nanophotonics group wouldn't be as effective and as exciting.

I would also like to thank all the staff of the cleanroom for their invaluable instructions on using the equipment without which, this thesis would have never seen the light of the day. I'd especially like to thank Mervi Koskinen, our Laboratory Engineer, for helping me day in and out with practically everything. I'd also like to thank Maria Bister, Marianna Raappana, Timo Aho, and Jarno Reuna for their assistance in the cleanroom. Last but not least, I would like to thank Dr. Turkka Salminen for teaching me how to use the Scanning electron microscope. I feel fortunate enough for just being able to use SEM, which I must admit was the most exciting task during my research.

Tampere, 1.6.2018

Aashish Sah

TABLE OF CONTENTS

LIST OF FIGURES

LIST OF ABBREVIATIONS AND SYMBOLS

SP	Surface plasmons
EM	electromagnetic
NS	nanostructures
SPP	Surface-plasmon polariton
LSP	Localized surface plasmon
EBL	Electron-beam lithography
AFL	Atomic-force lithography
BCP	Block copolymer
DSA	Directed self-assembly
SPR	Surface-plasmon resonance
NIL	Nanoimprint lithography
FDTD	Finite-difference time domain
SEM	Scanning Electron Microscopy
LSPR	Localized surface plasmon resonance
SW	Surface waves
MP	Magnetic plasmons
NP	Nanoparticle
TE	Transverse Electric mode
TM	Transverse Magnetic mode
UV	Ultra-Violet
MIF	Metal-ion free
PMGI	polymethylglutarimide
RIE	Reactive-ion etching
PS	polystyrene
P2VP	polyvinyl pyridine
THF	tetrahydrofuran
SVA	Solvent Vapour Annealing
RF	Radio-frequency
CEM	Computational electromagnetics
IE	Integral equation
DE	Differential equation
ICP	Inductively coupled plasma
SCCM	Standard Cubic Centimeters per Minute
TUT	Tampere University of Technology

1. INTRODUCTION

Plasmonics is an enticing field of nanophotonics that deals with the generation, control and manipulation of light by utilizing nano-scale structures and features. Surface plasmons (SPs), an integral part of plasmonics, investigate the interaction between electromagnetic (EM) waves and the conduction band electrons on a metal surface or in metal nanostructures (NSs). This interaction leads to the confinement of EM field over dimensions that are comparable to or smaller than the wavelength of light [1]. Based on the nature of interaction, SPs give rise to propagating and non-propagating coupled EM waves namely, surface plasmon polaritons (SPPs) and localized surface plasmons (LSPs). Interesting phenomena such as light localization and its enhancement are observed when the interaction takes place. These phenomena have opened up a wide range of exciting possibilities that have the potential to bring radical changes in the communication, energy harvesting, sub-wavelength imaging, and sensing technologies.

A plethora of nanotechnology industries have already been exploiting the market for decades with their label-free biosensing, sub-wavelength imaging microscopy, and other plasmonics based devices. The fabrication of the metallic NSs for these plasmonic devices relies on lithography techniques like electron-beam lithography (EBL), atomic-force lithography (AFL), optical lithography and other top-down or bottom-up lithography methods. These current lithography techniques provide some difficulties either due to the diffraction limit or are unfeasible for nanopatterning of uniformly dense structures over large-area. The goal of this thesis is to utilise block copolymer (BCP) lithography together with conventional lithography for hierarchical nanopatterning in the sub-wavelength regime for plasmonic applications.

BCPs are di-block polymer chains that can self-assemble into periodic nanopatterns under favourable conditions. The self-assembly of the polymer chains can be controlled or manipulated by introducing large diffracting structures as guiding templates that allows the BCPs to self-assemble only in certain directions. This directed self-assembly (DSA) of polymer chain into an ordered morphology provides an astonishing approach for large-area nanofabrication. Motivated by the simplicity of BCP lithography and

its sub-wavelength resolution, this thesis work investigates the combined effects of SPPs and LSPs. This hybridization of SPPs and LSPs may provide foreground for making better sensors and highly absorbing plasmonic coatings via strong electric field enhancement.

The content of the thesis is spanned over four distinct chapters. A brief theory on SPs is covered in *Chapter 2*. SPPs and LSPs are two important consequences of SPs that describe how light can be squeezed into dimensions smaller than its wavelength in plasmonics structures. This can lead to strong enhancement of the EM field. The chapter also focuses on different methods that can be used to excite surface plasmon resonance (SPR) and explains how these excitations can be observed experimentally.

As described in *Chapter 2*, SPPs and LSPs are supported only at metal-dielectric interface and in metal NSs respectively. Different methods that were employed to fabricate these metal NSs are discussed in *Chapter 3*. A short theory on the working principle of photolithography, nano-imprint lithography (NIL), and BCP lithography is presented along with a method, template-stripping, to transfer the pattern from a dielectric substrate to noble metal, gold (Au). A description of numerical scheme, finite-difference time domain (FDTD), used to simulate the interaction between light and metal NSs is studied.

An agreement between the theoretical and the experimental results is analysed in *Chapter 4*. Several diffracting structures are realized using the lithography processes detailed in *Chapter 3*. These diffracting structures are used as guiding templates for the DSA of block copolymers. The scanning electron microscope (SEM) images of these fabricated metal NSs are shown. The hybridization of SPPs and LSPs is investigated with the help of optical measurement and numerical analysis. The results from optical measurement provide the existence of SPR and localized surface plasmon resonance (LSPR) as a dip near plasmon resonance wavelength in the reflection spectrum whereas, results from numerical analysis help visualize the field enhancement in these metal NSs.

In *Chapter 5*, the consequences of the results shown in *Chapter 4* are carefully examined and discussed. The feature sizes of the metal structures fabricated using different lithography techniques are compared. The extreme light localization and enhancement in different metal NSs due to the combined effect of SPR and LSPR are analysed. Finally, the work is concluded with some discussions on possible directions that this research could take to exploit BCP lithography for nanofabrication.

2. THEORETICAL BACKGROUND

2.1 Surface Waves (SW)

A surface wave is just like any other wave but propagates along the interface between two distinct media. In optics, a surface wave is an electromagnetic wave that travels along the interface of two media that have differing dielectric constants [2]. The amplitude of this surface wave decays exponentially in the direction perpendicular to the direction of propagation. Depending on the permittivity or permeability of interfaces, the SWs are categorized into well-known types such as SPs, Magnetic Plasmons (MP), Surface Solitons and Dyakonov surface waves among others [2]. As motivated by the myriad of the application resulting from light localization, SPs are an interesting research topic in the nanophotonics community and will form the basis for this thesis work.

2.2 Surface plasmons

From Fermi-Dirac statistics, it was established that metals have free electron gas density from the electrons in the conduction band i.e. electrons with energy above the Fermi level. When subjected to an external electromagnetic field, this free electron gas density exhibits oscillating electron clouds in the vicinity of a metal nanoparticle (NP).

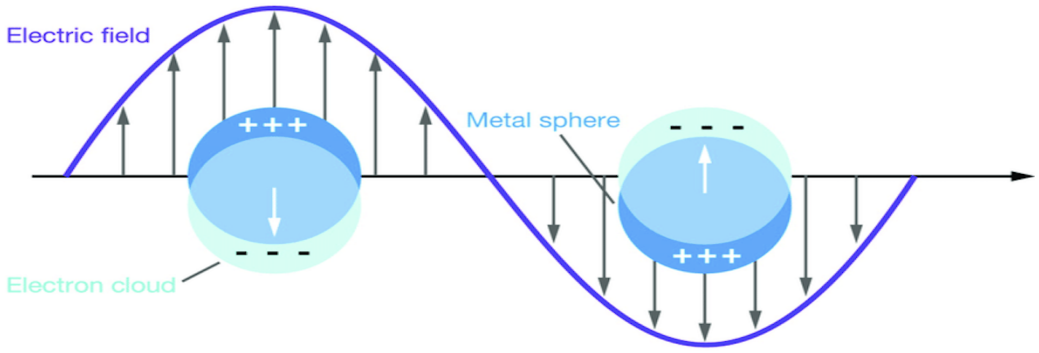

Figure 2.1 *Electric field of incident EM wave inducing electron cloud on the surface of metal NP [9].*

As shown in **Figure 2.1**, a charge cloud separation on the surface of the metal nanosphere induces an electric field, which cancels the electric field generated by the EM wave. Again, the electric field from the EM wave separates the charge cloud and the process continues, resulting in the oscillation of the free electron gas density. The quantum of this collective oscillation of the free electron gas density stimulated by external EM field is called plasmon [3].

SPs are collective oscillations of free electron gas that is supported at the metal-dielectric interface or on the surface of a metal NP. Not all metals and dielectrics will support this collective oscillation, a consequence imposed by the solution of Maxwell's equation. The condition states that the real part of the permittivity of the dielectric must be positive while for the metal, it must be negative. In addition, the imaginary part of the permittivity of both media must be smaller in magnitude than the real part. This will be derived later in the section (the derivation of all the equations in **section 2** follow the approach presented in [1] unless stated otherwise).

The oscillation of the free electron gas results in resonance when the frequency of the EM wave matches the plasma frequency of the metal. The plasma frequency required for resonance can be derived from the equation of motion for free electron gas density using the plasma model. The equation of motion is expressed in the classical sense as,

$$m\ddot{\mathbf{x}} + m\gamma\dot{\mathbf{x}} = -e\mathbf{E} \tag{2.1}$$

where m = mass of the electron, $\gamma = \frac{1}{\tau}$ (τ = relaxation time of the free electron gas and γ = collision frequency), e = charge of the electron and the driving harmonic electric field has the form, $\mathbf{E} = \mathbf{E}_0 e^{-i\omega t}$ with angular frequency of ω.

The above equation is a second-order differential equation, which resembles the equation of motion for elastic springs or pendulums. The solution to this equation together with its contribution to the macroscopic polarization yields an expression for electric displacement vector $\mathbf{D}$,

$$\mathbf{D}(\omega) = \epsilon_0 \mathbf{E}\left(1 - \frac{\omega_p^2}{(\omega^2 - i\gamma\omega)}\right) \tag{2.2}$$

where $\omega_p = \frac{ne^2}{\epsilon_0 m}$ is the plasma frequency of the free electron gas, n = number density of the free electron for a given metal, and ϵ_0 = permittivity of the free space. For noble metals such as gold, silver, copper, and aluminium, the plasma frequency

is in the visible range. Gold and silver are predominantly used for the study of surface plasmons. In order to excite a resonance on the surface of a noble metal, an EM wave with a frequency that matches the plasma frequency is required. Since frequency is just a constant times reciprocal of wavelength, an EM wave with a wavelength corresponding to the plasma frequency can be chosen for the excitation of the resonance.

Equation (2.2) also gives the complex dielectric function $\epsilon(\omega)$ of the metal since, $\mathbf{D} = \epsilon_0\epsilon(\omega)\mathbf{E}$,

$$\epsilon(\omega) = \left(1 - \frac{\omega_p^2}{(\omega^2 - i\gamma\omega)}\right) \tag{2.3}$$

The real part of the dielectric function for $\omega < \omega_p$ approximates to,

$$Re[\epsilon(\omega)] = 1 - \frac{\omega_p^2}{\omega^2} \tag{2.4}$$

This approximation of dielectric function of metal is known as the Drude model and is found to be a good approximation for quite many applications.

2.2.1 Surface Plasmon Polaritons

An interesting phenomenon is observed when the incident EM wave is coupled with the collective oscillation of the free electrons on the surface of noble metals. This only happens when the frequency of the incident EM wave matches the plasma frequency of the metal. The resulting SPR excites SPP modes that propagate along the interface with its amplitude decaying exponentially perpendicular to the interface i.e. the SPP is a "2D" EM wave confined to the interface. The propagating surface wave also vanishes after some distance along the interface, as energy is lost to absorption or scattering.

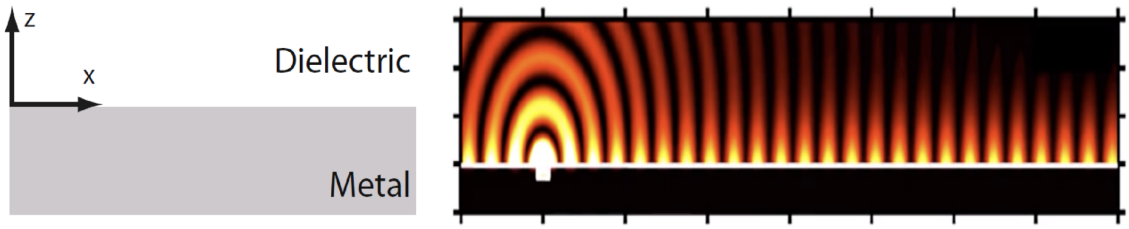

Figure 2.2 *Left) Geometry of the metal-dielectric system [1], Right) Propagating SPP at metal-dielectric interface [10].*

The exponentially decaying strongly enhanced EM field is a consequence from the

solution to Maxwell's equation for metal-dielectric interface. Maxwell's equation in differential frequency domain form can be expressed as,

$$\nabla \cdot (\epsilon \mathbf{E}) = 0, \tag{2.5}$$

$$\nabla \cdot \mathbf{H} = 0, \tag{2.6}$$

$$\nabla \times \mathbf{H} = i\omega\epsilon\mathbf{E}, \tag{2.7}$$

$$\nabla \times \mathbf{E} = -i\omega\mu\mathbf{H}, \tag{2.8}$$

From the curl equation (2.8), one can derive the wave equation,

$$\nabla^2\mathbf{E} + k_0^2\epsilon\mathbf{E} = 0, \tag{2.9}$$

The harmonic electric field propagates in x-direction with propagation constant β therefore, the electric field has the form $\mathbf{E}(x, y, z) = \mathbf{E}(z)e^{i\beta x}$. Solving equation (2.8) with this criteria yields,

$$\frac{\partial^2\mathbf{E(z)}}{\partial z^2} + (k_0^2\epsilon - \beta^2)\mathbf{E(z)} = 0, \tag{2.10}$$

The curl equation (2.8) together with ($\frac{\partial}{\partial y} = 0$) for the geometry shown in figure and for the propagation along the x-direction ($\frac{\partial}{\partial x} = i\beta$) yields,

$$\frac{\partial E_y}{\partial z} = -i\omega\mu_0 H_x, \tag{2.11}$$

$$\frac{\partial E_x}{\partial z} - i\beta E_z = i\omega\mu_0 H_y, \tag{2.12}$$

$$i\beta E_y = i\omega\mu_0 H_z, \tag{2.13}$$

$$\frac{\partial H_y}{\partial z} = i\omega\epsilon_0\epsilon E_x, \tag{2.14}$$

$$\frac{\partial H_x}{\partial z} - i\beta H_z = -i\omega\epsilon_0\epsilon E_y, \tag{2.15}$$

$$i\beta H_y = -i\omega\epsilon_0\epsilon E_z, \tag{2.16}$$

The geometry of metal-dielectric medium is shown in the **Figure 2.2** with permittivity dependence of $\epsilon_1 = \epsilon_1(z)$ and $\epsilon_2 = \epsilon_2(z)$ for dielectric and metal media respectively. The above system of equations can be solved using either transverse electric (TE) or transverse magnetic (TM) polarization of the EM field. It can be easily shown that the solution only exists for TM-polarized incident light i.e. SPPs only exist for TM polarization, where only the field components E_x, E_z and H_y are nonzero. E_x and E_z is expressed in terms of H_y using equation (2.11) and (2.13),

$$E_x = -i\frac{1}{\omega\epsilon_0\epsilon}\frac{\partial H_y}{\partial z}, \tag{2.17}$$

$$E_z = -\frac{\beta}{\omega\epsilon_0\epsilon}H_y, \tag{2.18}$$

The wave equation for TM polarization yields,

$$\frac{\partial^2 H_y}{\partial z^2} + (k_0^2\epsilon - \beta^2)H_y = 0, \tag{2.19}$$

The solution to equation (2.19) for dielectric-metal media yields,

$$H_y(z) = A_2 e^{i\beta x} e^{-k_2 z}, \tag{2.20}$$

$$E_x(z) = iA_2 \frac{1}{\omega\epsilon_0\epsilon_2} k_2 e^{i\beta x} e^{-k_2 z}, \tag{2.21}$$

$$E_z(z) = -A_2 \frac{\beta}{\omega\epsilon_0\epsilon_2} e^{i\beta x} e^{-k_2 z}, \tag{2.22}$$

$$H_y(z) = A_1 e^{i\beta x} e^{k_1 z}, \tag{2.23}$$

$$E_x(z) = -iA_1 \frac{1}{\omega\epsilon_0\epsilon_1} k_2 e^{i\beta x} e^{k_1 z}, \tag{2.24}$$

$$E_z(z) = -A_1 \frac{\beta}{\omega\epsilon_0\epsilon_1} e^{i\beta x} e^{k_1 z}, \tag{2.25}$$

The exponential term in z-direction in both medium shows that field is decaying perpendicular to the interface as discussed earlier. The continuity of $\mathbf{E}_{1,2z}$ at the interface gives $A_1 = A_2$, and continuity in $\mathbf{E}_{1,2x}$ yields,

$$\frac{k_2}{k_1} = -\frac{\epsilon_2}{\epsilon_1}, \tag{2.26}$$

Equation (2.25) imposes that the $Re[\epsilon_1] < 0$ while $Re[\epsilon_2] > 0$ and $Im[\epsilon_{1,2}] < Re[\epsilon_{1,2}]$. Noble metals and any dielectric fulfil these conditions hence, supporting SPP.

Continuity in $H_{1,2}y$ has to fulfil the wave equation (2.19) and thus yields,

$$k_1^2 = \beta^2 - k_0^2\epsilon_1, \tag{2.27}$$

$$k_2^2 = \beta^2 - k_0^2\epsilon_2, \tag{2.28}$$

The dispersion relation of SPPs propagating at the metal-dielectric interface is determined by combining equation (2.26) - (2.28),

$$\beta = \frac{\omega}{c}\sqrt{\frac{\epsilon_1\epsilon_2}{\epsilon_1+\epsilon_2}} = k_0\sqrt{\frac{\epsilon_1\epsilon_2}{\epsilon_1+\epsilon_2}} \tag{2.29}$$

where β is the propagation constant of the surface plasmon polariton, $k_0 = \frac{\omega}{c}$ is the wave number of the propagating wave in vacuum, ϵ_1 and ϵ_2 works for both the complex and real form of dielectric function. The characteristic dispersion relation of gold-air and silver-air interfaces are shown below.

From the dispersion relation shown in **Figure 2.3** and **2.4**, it can be observed that the SPP excitation is only possible for the dispersion curve that lies on the right side of the light line (for frequencies less than or equal to plasma frequency). The propagation constant of SPP, β, is greater than the wave number, k_0, of a light wave in air. This difference in the propagation constant and wavenumber of light obstructs the excitation of SPP modes at the dielectric-metal interface by a simple

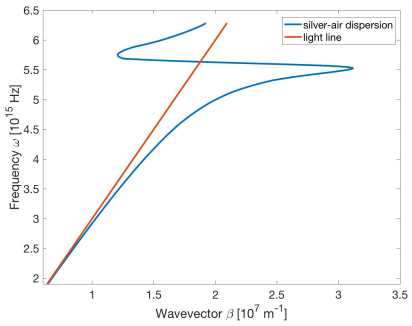

Figure 2.3 *Dispersion relation of SPPs at a silver/air interface.*

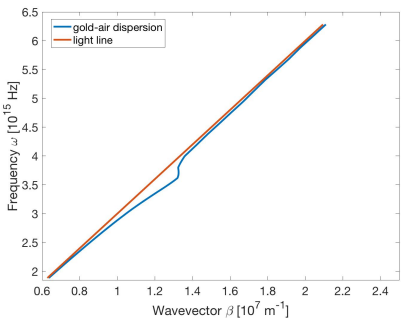

Figure 2.4 *Dispersion relation of SPPs at a gold/air interface.*

illumination of light [1]. Special phase-matching techniques need to be employed to overcome this difference.

Numerous optical/photon excitation and observation methods of SPPs have been developed to overcome the momentum's mismatch by increasing the momentum of incident light. Prism coupling and Grating coupling are the most common methods. Otto configuration and Kretschmann configuration are two most used prism coupling methods. These prism coupling schemes induce evanescent waves at the metal-dielectric interface due to total internal reflection. These evanescent waves have enough momentum to excite the SPR. Examples of two typical prism coupling schemes: Otto and Kretschmann configurations are shown in **Figure (2.5)**.

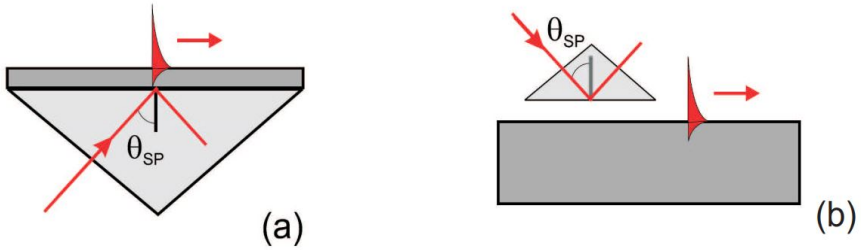

Figure 2.5 *Prism coupling: (a) Kretschmann, (b) Otto configuration [5].*

Grating coupling overcomes the difference in the in-plane impinging wavevector $ksin\theta$ and propagation constant β of SPP modes by introducing diffraction patterns on the metal film with some periodicity $\wedge$ [1].

The grating coupling yields the condition for phase matching,

$$\beta = k \sin\theta \pm m\frac{2\pi}{\wedge} \tag{2.30}$$

where θ is the incident angle of the light, $\wedge$ is the periodicity of the grating and

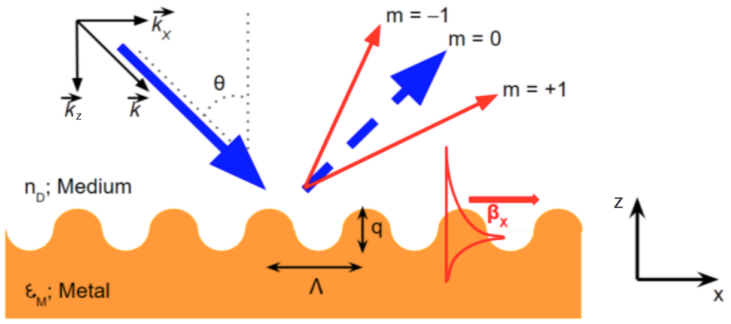

Figure 2.6 *Grating coupling scheme for the excitation of SPPs [11].*

$m = 0, \pm 1, \pm 2, \pm 3...$ is the diffraction order. Whenever condition (2.30) is satisfied, the excitation of SPP takes place.

From condition (2.29), the periodicity of the grating can be defined for a given wavelength λ of the impinging light for phase matching,

$$\wedge = \frac{m\lambda}{|n_{eff} - \sin\theta|} \tag{2.31}$$

It can be seen from equation (2.30) that for order $m = 1$, the grating periodicity is comparable to the wavelength of the incident light, $\lambda \approx \wedge$. The excitation of SPP can be observed as a minimum in the reflection measurement of the metal-dielectric system with the gratings. The minimum is observed at λ as a result of the phase-matching condition.

2.2.2 Localised Surface Plasmon

Contrary to SPPs, LSPs are non-propagating excitations of EM waves coupled with plasmons on the surface of metal NP [1]. The external field induces a collective oscillation of the conduction band electrons in metal NPs at a certain wavelength. The plasmon resonance on the curved surface of the metal NPs couples to the external EM field and excites LSPR. This also results in field amplification inside and outside the metal NP.

The interaction of light with a metal NP can be described by the *Quasi-static approximation*, which states that if the size of the metal NP is much less than the wavelength of light i.e. $d << \lambda$. Under this approximation, a constant Electric field in z-direction is defined as $\mathbf{E} = E_0\hat{z}$. Surrounding medium with constant dielectric ϵ_m and the dielectric function of metal defined by Drude model, $\epsilon(\omega)$ is considered for a simple treatment of LSP.

With this electrostatic approach, one leads to the Laplacian $\nabla^2\Phi = 0$. Solving this Laplacian together with appropriate boundary condition and $\vec{E} = -\Phi$ in polar coordinates yields,

$$\mathbf{E}_{in} = \frac{3\epsilon_m}{\epsilon + 2\epsilon_m}\mathbf{E}_0, \tag{2.32}$$

$$\mathbf{E}_{out} = \mathbf{E}_0\left(1 - \frac{\epsilon - \epsilon_m}{\epsilon + 2\epsilon_m}\frac{a^3}{r^3}\right), \tag{2.33}$$

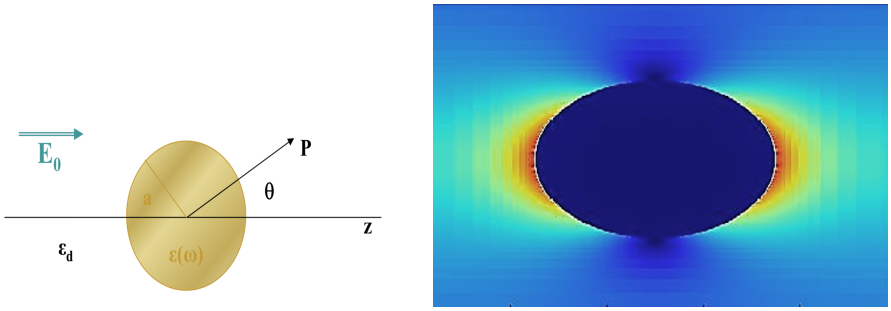

Figure 2.7 *Left) Polar coordinate choice for geometry of LSP [1], Right) non-propagating strong field enhancement due to LSP excitation.*

From equation (2.33), it can be observed that the field enhancement outside the metal nanosphere occurs if the denominator $|\epsilon + 2\epsilon_m|$ is minimum. This results in the condition,

$$Re[\epsilon(\omega)] = -2\epsilon_m, \tag{2.34}$$

This relationship is known as Fröhlich condition. If the dielectric medium is assumed to be air, $\epsilon_d = 1$, the resonance frequency can be found by,

$$1 - \frac{\omega_p^2}{\omega^2} = -2 \implies \omega_0 = \frac{\omega_p}{\sqrt{3}} \tag{2.35}$$

Whenever this condition is met, the excitation of LSPR results in strong localized electric field as shown in **Figure 2.7 (right)**. It can be observed from equation (2.35) that the excitation of LSPR doesn't require any phase matching schemes and the existence of LSPR can be measured as an absorption peak in the spectra. One can control the position of the peak by varying metal NP size, shape or by altering the local environment.

3. RESEARCH METHODOLOGY AND MATERIALS

As explained in **section 2.2.1**, excitation of SPR at a metal/dielectric interface is done via the grating coupling method. Periodic structures were realized using photolithography and NIL. For the excitation of LSPR, sub-wavelength metal NSs were fabricated utilising DSA of block copolymers. The lithography techniques associated for the fabrication of these metal NSs are explained briefly in this section.

3.1 Photolithography (Image Reversal)

Photolithography is a **microfabrication** process that allows the transfer of geometric patterns to an underlying substrate. A mask with cut-outs of the desired geometric shapes controls the photo/light exposure of a photosensitive thin film on a substrate. The photosensitive chemical is called "photoresist" or just "resist". Depending on the requirement, either a positive or a negative resists is used. For image reversal photolithography, negative resist is used. A schematic of the different steps involved in the photolithography technique is shown in **Figure 3.1**.

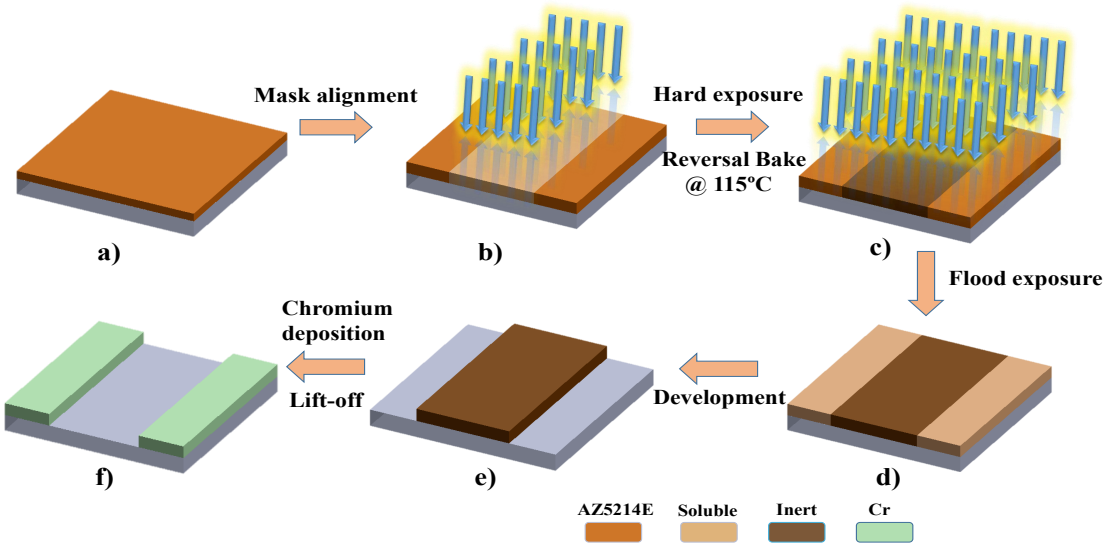

Figure 3.1 *A schematic of photolithography microfabrication process.*

Suss MicroTec MA6 mask aligner is used for the photolithography process. Lab-grade

polished, single-crystal Si substrates with (100) orientation, and p-type doping were used without any further modifications for patterning. The steps involved with the microfabrication process is described below:

- A photo-sensitive resist, AZ 5214E, is spin-coated on top of a Si substrate at 4000 RPM for 40s and then it is heated on a hotplate at 100 °C for 60s, **Figure 3.1 (a)**.
- The desired photomask is placed on a mask holder through which the resist is exposed. The substrate is then aligned underneath the photomask.
- The resist is exposed to ultraviolet (UV) light where it is allowed by the photomask (middle of the substrate in **Figure 3.1 (b)**. The exposed area is now soluble in a resist removal chemical, metal-ion free (MIF) developer AZ 726.
- The substrate is heated on a hotplate at 115 °C for 2 minutes. This process, image reversal bake, cross-links the exposed area, making the soluble area now **inert** to MIF AZ 726 while the unexposed remains photo-active as shown in **Figure 3.1 (c)**.
- The substrate is again placed inside the mask aligner but without the photomask. The whole substrate is exposed to UV light **Figure 3.1 (c)**, making the photo-active resist soluble in MIF AZ 726. This is shown as a change in colour contrast in **Figure 3.1 (d)**.
- The substrate is then dipped in the resist removal solution. This step removes everything but the cross-linked resist in the middle as seen in **Figure 3.1 (e)**.
- A thin layer of chromium is evaporated onto the substrate using e-beam thermal evaporation. The chromium on top of the resist is lifted off using Acetone and 2-propanol in an ultrasonic bath. Finally, a chromium line grating is achieved with a periodicity of 4 microns and line width of 2 microns as depicted in **Figure 3.1 (f)**.

3.2 Nanoimprint Lithography

Nanoimprint Lithography is a **nanopatterning** technique that allows the fabrication of NSs with a feature size of tens to hundreds of nanometers. NIL utilises the similar

idea of transferring patterns from a master template to an underlying substrate as photolithography but with slight variations in the process steps. NIL can further be classified into two types: Thermal-NIL and UV-NIL. In Thermal-NIL, the master template imprints the pattern onto a heated thermoplastic polymer whereas, UV-NIL requires UV-curable polymers for imprinting of the patterns from master template under UV light exposure [7].

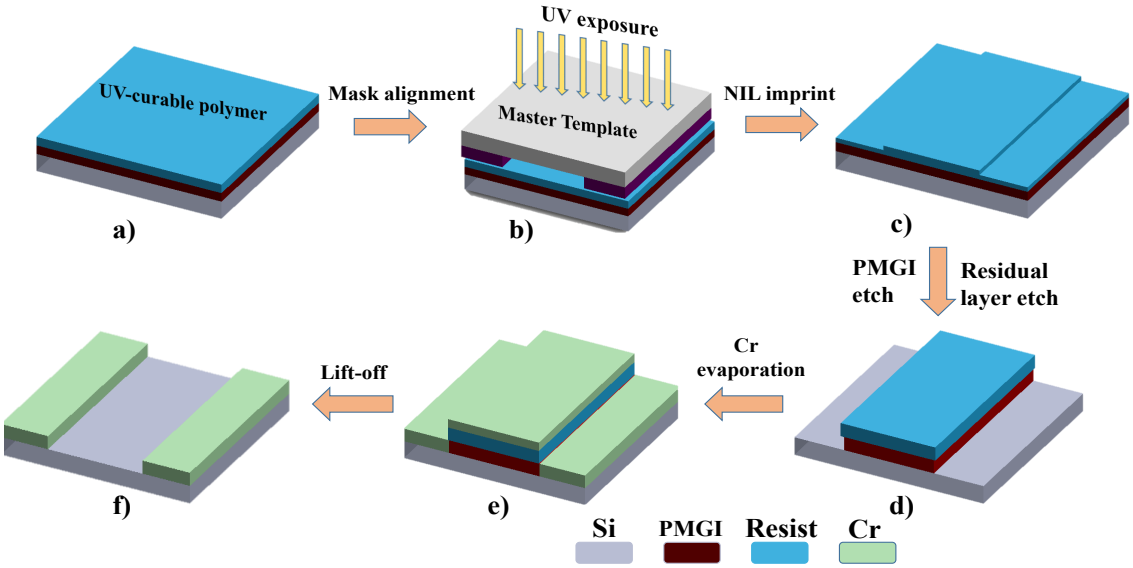

Figure 3.2 *A schematic of UV-NIL nanofabrication process.*

EVG 620 mask aligner is used for UV-NIL. Steps associated with the NIL nanofabrication are as follows:

- A thin layer of polymethylglutarimide (PMGI) is spin-coated at 4000 rpm for 60s on top of a Si substrate and then heated at 225 °C for 60s. After this, a UV-sensitive NIL resist is spin-coated on top of the PMGI layer at 3000 RPM for 40s and heated at 80 °C for 60s, **Figure 3.2 (a)**.
- NIL stamp (master template) with the desired topographic pattern is placed on the mask holder and the substrate is placed underneath the mask. The mask is pressed into the resist and the resist is exposed to UV light. UV exposure cross-links the resist to preserve the pattern obtained during imprinting, this step can be seen in **Figure 3.2 (b)** and **Figure 3.2 (c)**.
- After the imprinting, the "residual layer" (excess of UV-NIL resist) needs to be removed. This is done by etching the resist with ionized oxygen gas using

reactive-ion etching (RIE). Residual PMGI underneath the UV-NIL resist is etched away using MIF developer AZ 726. The result is shown in **Figure 3.2 (d)**.

- A thin layer of chromium is evaporated onto the substrate using e-beam thermal evaporation. The chromium on top of the PMGI and resist is lifted off using heated resist remover S-1165 in an ultrasonic bath. Finally, a chromium line grating is achieved with a periodicity of 405 nm and line width of 105 nm, as depicted in **Figure 3.2 (f)**.

3.3 Block copolymer lithography

BCP lithography is a bottom-up nanofabrication process that has attracted a lot of attention in the nanotechnology industry in recent years as an alternative patterning technology for attaining feature sizes of tens of nanometers. BCPs are an ensemble of two or more distinct blocks of monomers linked together via covalent bonds [4]. Some of the typical block copolymers with different arrangements of the monomer segments can be seen in **Figure 3.3**.

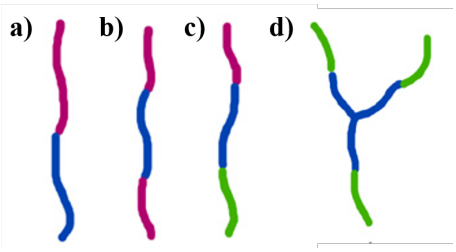

Figure 3.3 *a) AB linear diblock, b) ABA linear triblock, c) ABC linear triblock, and d) BC starblock [4].*

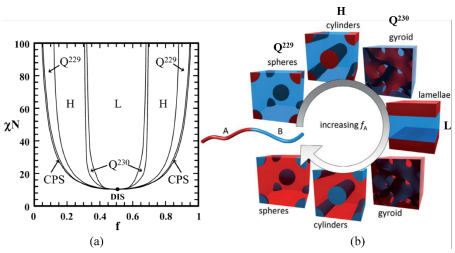

Figure 3.4 *a) Phase diagram of diblock polymer, and b) Different shapes of the morphology as a function of volume fraction ratio f [5].*

One of the key features of BCPs is the self-assembly of the monomer blocks into ordered periodic patterns. The monomer blocks are immiscible together and therefore, they phase separate to form distinct microdomains. The domain shapes and the periodicity depend on the molecular weight of the BCP and the volume fraction of the monomers. The domain shapes for various morphologies are described by the phase diagram shown in the **Figure 3.4**. The BCP morphology depends on the volume fraction of the monomer blocks f, the Flory-Huggins interaction parameter χ, and the degree of polymerization N. In the phase diagram, above the parabola

curve, morphologies such as hexagonally-packed cylinders, lamellae and close-packed spheres can be obtained depending on the BCP volume fraction [4].

The BCP of interest for this thesis work is a diblock copolymer poly(styrene-b-2-vinyl pyridine) (PS-b-P2VP) with a molecular weight of 188000 g/mol and a PS volume fraction of 0.73. For this BCP, the phase diagram dictates hexagonally-packed cylinder as the equilibrium morphology.

Self-assembly of this (PS-b-P2VP) on a bare Si substrate results in hexagonally-packed cylinders that form grains with similar packing orientation. The orientation and organization of the patterns can be controlled by introducing a guiding template [6]. This guiding template directs the assembly of the BCP on the substrate hence, called "Directed self-assembly". Here, a topographic guiding template is fabricated using photolithography (described in **section 3.1**) and NIL (described in **section 3.2**). The schematic for the process flow of BCP lithography together with template-stripping is shown in **Figure 3.5**.

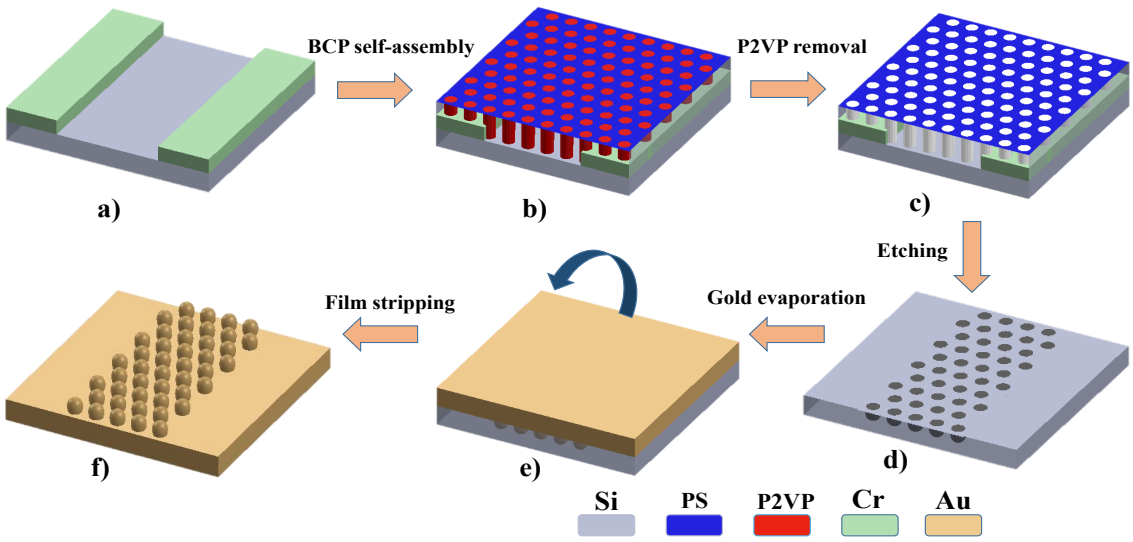

Figure 3.5 *A schematic of BCP Lithography process for sub-wavelength metal NSs.*

A guiding template was fabricated for DSA of the BCP using one of the conventional lithography techniques described in **sections 3.1** and **3.2**. For plasmonics applications, UV-NIL is preferred over photolithography. PS-b-P2VP was purchased from Polymer Source Inc. and was used without any further treatment. A thin film of

BCP on the guiding template is required and therefore, an evident way to achieve this is to make a solution of BCP. A mixture of anhydrous tetrahydrofuran (THF) and toluene, purchased from Sigma-Aldrich, was used as the solvent. The ratio for the solvent blends was determined using Hansen solubility parameters (HSPs) using [7]. These parameters are energy from dispersion forces, intermolecular forces, and hydrogen-bonding between molecules (δ_D, δ_P, and δ_H resp.) and they measure an optimized ratio of blends for two different solvents that is effective to dissolve certain molecules [7]. For PS, a ratio of 30:70 (THF: Toluene) was found appropriate for dissolving the high molecular weight di-block copolymer, PS-b-P2VP. A 1.0 w/v-% solution was left to stir overnight at room temperature.

A SSE OPTIcoat spinner was used to spin-coat the BCP solution on the guiding template with the lid closed at 3000 RPM for 40s. This resulted in a film thickness of $44 - 50$ nm. Immediately after the spin-coating, the substrate was placed on a hot-plate at 125 °C for 2 min to evaporate the excess solvent. Solvent-vapor annealing (SVA), a process of controlled swelling of the BCP film under THF vapour for 5 min, resulted in a hexagonally-packed cylinder morphology with a center-to-center distance of 75 nm. The PS and P2VP phase separates into micro domains as seen in **Figure 3.5 b** with P2VP domains as red cylinders and PS domains as blue region.

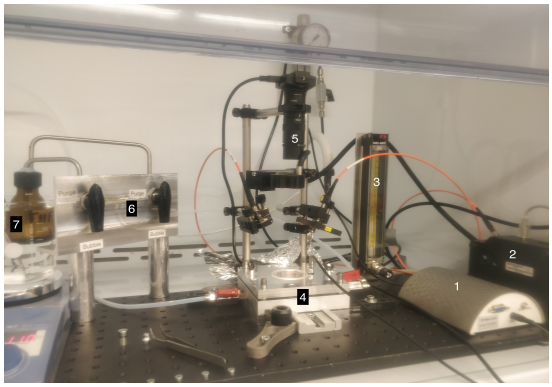

Figure 3.6 *SVA setup.*

Self-assembly of the BCPs can be achieved simply by placing the substrate in a jar with the solvents for some time. However, a controlled swelling is favoured and utilised for self-assembly of the BCPs in this work. This is made feasible by using SVA setup as shown in **Figure 3.6**. The SVA setup includes an optical setup that requires light source (1) and detector (2) for controlling the swelling ratio and a camera (5) to monitor the changes in the film during the annealing process. The substrate is placed on top of the heat-plate that is inside the chamber (4). The heat-plate facilitates the temperature change required during the process. The solvent is kept in the jar (7) and the vapour flow is controlled by the knobs on the plate (6). Pressure-gauge meter (3) is used to set the flow rate

of the N_2 and thus the solvent vapour for annealing process. The SVA process is monitored and guided by the control files developed on the MATLAB.

Ethanol was used to selectively swell P2VP domains and open up pores in the BCP film. The substrate was kept in a heated ethanol at 50 °C for 5 min, resulting in hollow nanopores hollow as seen in **Figure 3.5 c**. These self-assembled hexagonally-packed cylindrical pores could now be used as a dry etch mask. The BCP pattern was dry etched into Si using RIE in sulfur hexafluoride and oxygen plasma with radio-frequency (RF) power 160 W, flow rate of 12/9 sccm for SF6/O2, and pressure of 30 mTorr. The etch time varied from 18s to 23s. The diameter of the nanopores depended on the etch time and varied from 45 to 55 nm (**Figure 3.5 d**).

The end goal was to transfer the pattern into noble metals. This was achieved by depositing a 150 nm of Au film on top of the nanoporous Si template, **Figure 3.5 e**. Since, the adhesion between gold film and Si is quite weak, the gold film could be stripped off from the nanoporous Si template using UV-curable glue. A droplet of UV-curable glue was spread on top of the gold film. A glass slide was placed on top of the glue and cured inside an UV oven for fascilitating adhesion between the glass and Au film. The glass was lifted off from the nanoporous template. This resulted in the transfer of the pattern into a gold film as depicted in **Figure 3.5 f**.

3.4 Numerical Simulation

Computational electromagnetics (CEM) is a set of numerical methods that model the interaction of the electromagnetic wave with matter by solving Maxwell's equation on a given geometry with appropriate boundary conditions. Among many numerical schemes, integral equation (IE) methods and differential equation (DE) methods are prevalently used techniques for the simulation of electromagnetic problems. IE methods approximate the Maxwell's equations in integral form as finite sums, whereas DE methods approximate the Maxwell's equations in differential form as finite differences [8]. DE methods are used to simulate the electromagnetic interaction with the metal NSs in this thesis work.

Since, Maxwell's equation in differential form can be expressed in both time-domain and frequency-domain, one could use either of the domain for the finite difference scheme. It turns out that the frequency-domain solver requires more storage memory and is relatively slow compared to the time-domain solver. Therefore, finite-difference time domain (FDTD) scheme is employed in the numerical simulations of these

NSs. In addition, a frequency-domain solution can also be obtained by taking a fourier transform of the time-domain solution. The frequency-domain solution is particularly important in calculating Poynting vector and transmission/reflection of the electromagnetic wave in the structures.

3.4.1 Finite differences

In order to compute a derivative of a function numerically, one needs to discretise the domain of the function and then the derivative is approximated using its definition.

The analytical definition for the derivative of a function is,

$$f'(x) = \lim_{\Delta x \to 0} \frac{f(x + \Delta x) - f(x)}{\Delta x} \tag{3.1}$$

The derivative is approximated by relaxing the condition $\Delta x \to 0$ to some fixed nonzero fixed value for Δx. This Δx is now the difference between two consecutive discretised points from the domain space. The derivative of a function can now be approximated by,

$$f'(x) \approx \frac{f(x + \Delta x) - f(x)}{\Delta x} \tag{3.2}$$

$$f'(x) \approx \frac{f(x) - f(x - \Delta x)}{\Delta x} \tag{3.3}$$

Equation (3.2) is called ***forward-difference*** and equation (3.3) is called ***backward-difference***. Average of these two finite-difference schemes yields,

$$f'(x) \approx \frac{f(x + \Delta x) - f(x - \Delta x)}{2\Delta x} \tag{3.4}$$

$$f''(x) \approx \frac{f(x + \Delta x) - 2f(x) + f(x - \Delta x)}{(\Delta x)^2} \tag{3.5}$$

Equation (3.4) is first-order and equation (3.5) is a second-order ***central-difference*** approximation. This approximation is numerically stable and yields less error compared to forward and backward approximation. FDTD scheme will utilise the same central-difference approximation for solving Maxwell's equations numerically.

3.4.2 FDTD Method for solving Maxwell's equation

The differential time-domain Maxwell's equations that explain the behaviour of the electric and magnetic field over time are given by,

$$\nabla \cdot \mathbf{D} = \rho, \tag{3.6}$$

$$\nabla \cdot \mathbf{B} = 0, \tag{3.7}$$

$$\nabla \times \mathbf{H} = \frac{\partial \mathbf{D}}{\partial t}, \tag{3.8}$$

$$\nabla \times \mathbf{E} = -\frac{\partial \mathbf{B}}{\partial t}, \tag{3.9}$$

The equations that relate the Electric field strength $\mathbf{E}$ to electric displacement vector $\mathbf{D}$, and Magnetic field strength $\mathbf{H}$ to magnetic flux density $\vec{B}$ is known as constitutive relations and these relations together with curl equations (3.8) and (3.9) yields,

$$\mathbf{D} = \epsilon \mathbf{E}, \tag{3.10}$$

$$\mathbf{B} = \mu \mathbf{H}, \tag{3.11}$$

$$\nabla \times \vec{H} = \epsilon \frac{\partial \vec{E}}{\partial t}, \tag{3.12}$$

$$\nabla \times \vec{E} = -\mu \frac{\partial \vec{B}}{\partial t}, \tag{3.13}$$

where $\epsilon = \epsilon(x, y, z)$ is the permittivity of the medium and $\mu = \mu(x, y, z)$ is the permeability of the medium. FDTD algorithm only uses curl equations (3.12) and (3.13) for computational purposes. The algorithm takes care of the divergence equations (3.6) and (3.7) during the computational process.

The curl of a vector field is the measure of rotation of the field at any specific point, given by the direction of rotation and the magnitude of rotation. The curl of the vector field can be found by the cross-product between the gradient and the vector field. Maxwell's curl equations therefore extends to following six scalar equations:

$$\frac{\partial E_x}{\partial t} = \frac{1}{\epsilon_x}\left(\frac{\partial H_z}{\partial y} - \frac{\partial H_y}{\partial z}\right), \tag{3.14}$$

$$\frac{\partial E_y}{\partial t} = \frac{1}{\epsilon_y}\left(\frac{\partial H_x}{\partial z} - \frac{\partial H_z}{\partial x}\right), \tag{3.15}$$

$$\frac{\partial E_z}{\partial t} = \frac{1}{\epsilon_z}\left(\frac{\partial H_y}{\partial x} - \frac{\partial H_x}{\partial y}\right), \tag{3.16}$$

$$\frac{\partial H_x}{\partial t} = \frac{1}{\mu_x}\left(\frac{\partial E_y}{\partial z} - \frac{\partial E_z}{\partial y}\right), \tag{3.17}$$

$$\frac{\partial H_y}{\partial t} = \frac{1}{\mu_y}\left(\frac{\partial E_z}{\partial x} - \frac{\partial E_x}{\partial z}\right), \tag{3.18}$$

$$\frac{\partial H_z}{\partial t} = \frac{1}{\mu_z}\left(\frac{\partial E_x}{\partial y} - \frac{\partial E_y}{\partial x}\right), \tag{3.19}$$

These six equations are solved numerically using the central difference scheme for the Electric and Magnetic field strength for a given geometry. The electric and magnetic

field strength values are calculated from a discretised time and space domain. A well-known discretization of the space domain (Yee cell) has been formulated by Kane Yee for solving the Maxwell's equation [8]. The way Yee cell has been discretised is that the electric field component and magnetic field component are calculated half a cell apart $E_{x,y,z}$ in the middle of the edge and $H_{x,y,z}$ in the middle of the face of the Yee cell. as shown in the **Figure 3.7**. This Yee cell simulates the Faraday's law since, each component of **H** is surrounded by four **E** and vice-versa.

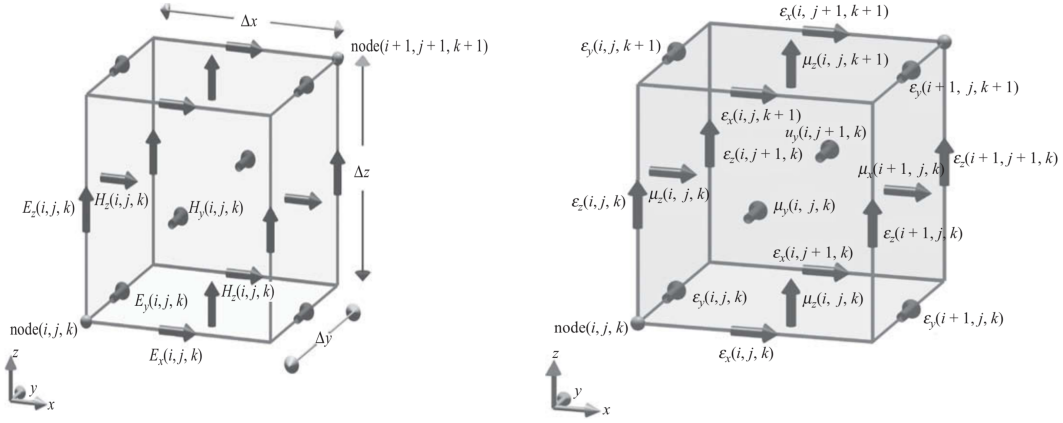

Figure 3.7 *Discretization of spatial domain (Yee cell) [8].*

The temporal domain is discretised uniquely for both fields, $(n+1)\Delta t$ for **E** and $(n+\frac{1}{2})\Delta t$ for **H**. E_x at position (i,j,k) can be approximated using the central difference scheme in equation (3.14). This yields,

$$\frac{E_x^{n+1}(i,j,k) - E_x^n(i,j,k)}{\Delta t} = \frac{1}{\epsilon_x(i,j,k)}\left(\frac{H_z^{n+\frac{1}{2}}(i,j,k) - H_z^{n+\frac{1}{2}}(i,j-1,k)}{\Delta y} - \frac{H_y^{n+\frac{1}{2}}(i,j,k) - H_y^{n+\frac{1}{2}}(i,j,k-1)}{\Delta z}\right) \tag{3.20}$$

From equation (3.20), the value of $E_x(i,j,k)$ for the next time step is updated and $E_x^{n+1}(i,j,k)$ has the value given by,

$$E_x^{n+1}(i,j,k) = \frac{\Delta t}{\epsilon_x(i,j,k)}\left(\frac{H_z^{n+\frac{1}{2}}(i,j,k) - H_z^{n+\frac{1}{2}}(i,j-1,k)}{\Delta y} - \frac{H_y^{n+\frac{1}{2}}(i,j,k) - H_y^{n+\frac{1}{2}}(i,j,k-1)}{\Delta z}\right) + E_x^n(i,j,k) \tag{3.21}$$

Similar steps can be taken to update the field values at new time stamps, giving $E_y^{n+1}(i,j,k)$, $E_z^{n+1}(i,j,k)$, $H_x^{n+\frac{1}{2}}(i,j,k)$, $H_y^{n+\frac{1}{2}}(i,j,k)$, and $H_z^{n+\frac{1}{2}}(i,j,k)$. The steps involved in FDTD algorithm can be summarized with the help of the following flowchart.

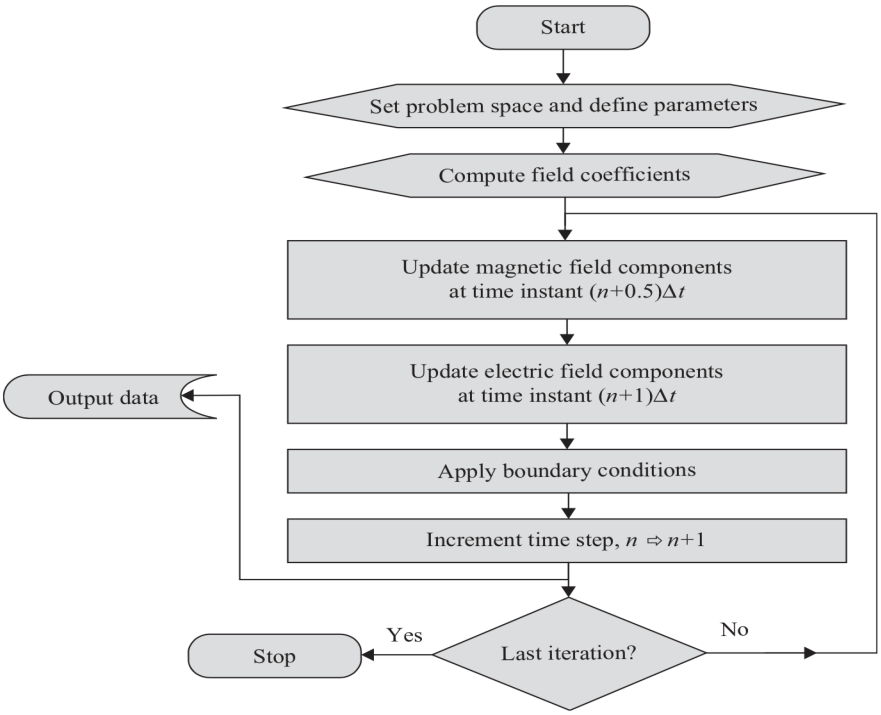

Figure 3.8 *FDTD Algorithm [8].*

3.4.3 Lumerical FDTD Solutions

A commercially available software, Lumerical FDTD solutions, was used for the simulation of the metal nanostructure in this thesis work. The implementation of the FDTD algorithm is the same as described in the previous section. One can easily implement an FDTD algorithm on Matlab or Python, however, defining the boundary conditions, geometric mesh, source and simulation space is quite difficult. In addition to this, visualizing results becomes a painstaking task. FDTD solutions, on the otherhand, is very flexible and intuitive to use. Complex and periodic geometries are easy to create and the implementation of convergence test is quite robust in FDTD solutions. It gives the user a freedom of choosing the mesh sizes, simulation space, source and allows different options for the visualization of the data.

4. RESULTS AND ANALYSIS

In this section, fabricated metal NSs using different lithography techniques described in **Chapter 3** are shown. Optical schemes mentioned in **Chapter 2** for the excitation of SPR and LSPR and their hybridization is studied and the results are presented. Investigation of the E-field enhancement in these structures are demonstrated with the help of numerical simulation demonstrated in **section 3.4** section. These simulations not only help visualize the interaction between light and matter but also help validate experimental results.

4.1 BCP lithography on micron-sized grating templates

Micron-sized diffracting structures were fabricated using the steps detailed in **section 3.1**. Line gratings of width 2 microns and a periodicity of 4 microns and square gratings of length 3 microns and a periodicity of 5 microns were fabricated and are shown in **Figure 4.1 (a)** depicting chromium regions as bright lines and **Figure 4.1 (b)** with Si areas as relatively dark squares.

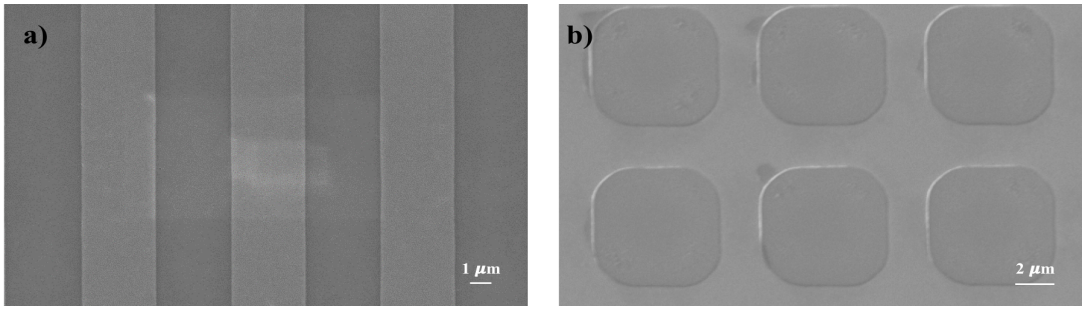

Figure 4.1 *a) Line gratings with line width of 2 microns and periodicity of 4 microns, b) Square gratings with length of 3 microns and periodicity of 5 microns.*

Line and square gratings were used as guiding templates for BCP directed self-assembly. The BCP lithography process described in **section 3.3** was used to fabricate Si templates and template-stripping method presented in the same section was utilised to transfer the patterns into the Au film. The experimental results are shown in the **Figure 4.2**. The hexogonally-packed hollow nanopores shown in **Figures 4.2 (a)** and **4.2 (d)** resulted from selectively swelling of P2VP domains

using ethanol. Si templates presented in **Figures 4.2 (b)** and **4.4 (e)** were prepared by first dry etching these nanoprores into Si and then removing the chromium areas, yielding BCP structures in only certain areas. The Si templates were then used for the fabrication of Au NSs via template-stripping.

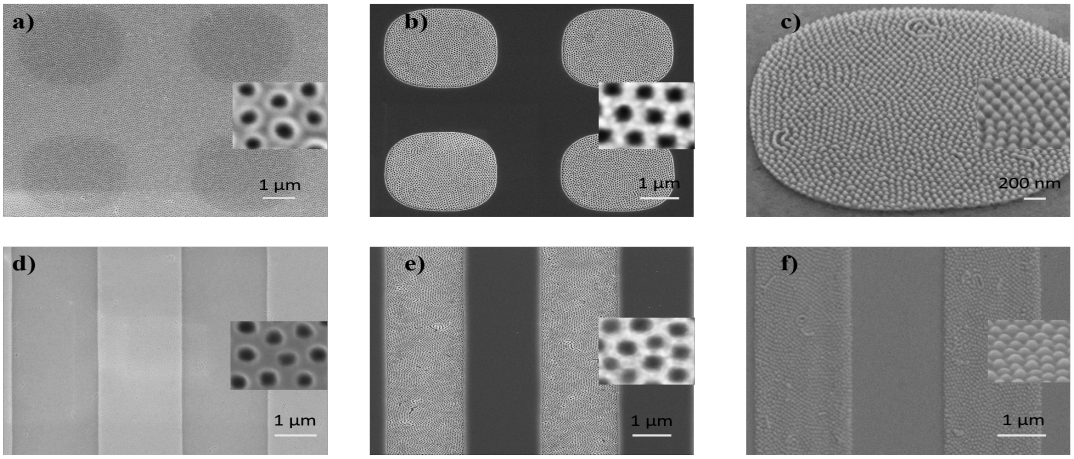

Figure 4.2 *(a) Hexagonally-packed cylinder morphology for square grating template, (d) for line grating template, (b,e) Dry etching of BCP nanopores mask into Si, and (c,f) Template stripped Au film.*

4.2 BCP lithography on nano-sized gratings

As explained in **section 2.2.1**, the first-order SPR dip in the reflection spectrum is seen at wavelength equivalent to the periodicity of the gratings. Nano-scale gratings allow for the observation of the dip in the visible range. Two nano-scale gratings were fabricated using UV-NIL as described in **section 3.2**. These gratings were used as the guiding templates and are shown in **Figure 4.3**. A 50 nm deep Si hole arrays and a 5 nm thick chromium disks are shown in **Figures 4.3 (a)** and **4.3 (b)**. Chromium disks were made by metal evaporation and lift-off processing whereas, the hole arrays were made by RIE and no metal deposition was needed.

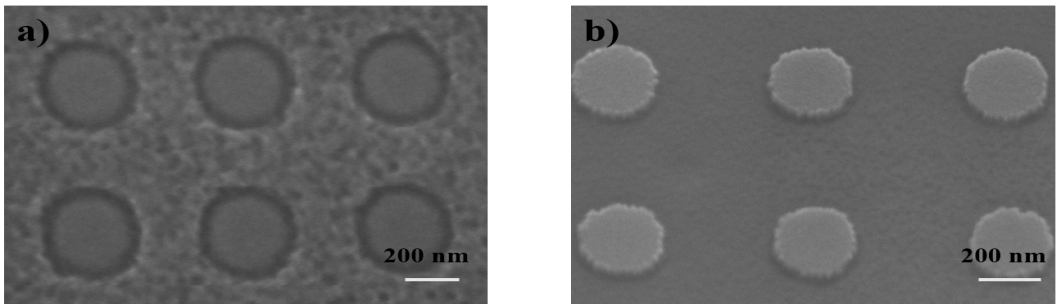

Figure 4.3 *a) Hole structures with diameter of 350 nm and periodicity of 650 nm, b) Nanodisks with diameter of 270 nm and periodicity of 600 nm.*

These two guiding templates were also used for the BCP directed-self assembly lithography. The BCP lithography process for these guiding structures and transferring of patterns into Au metal followed the same processes as explained in **section 3.3**.

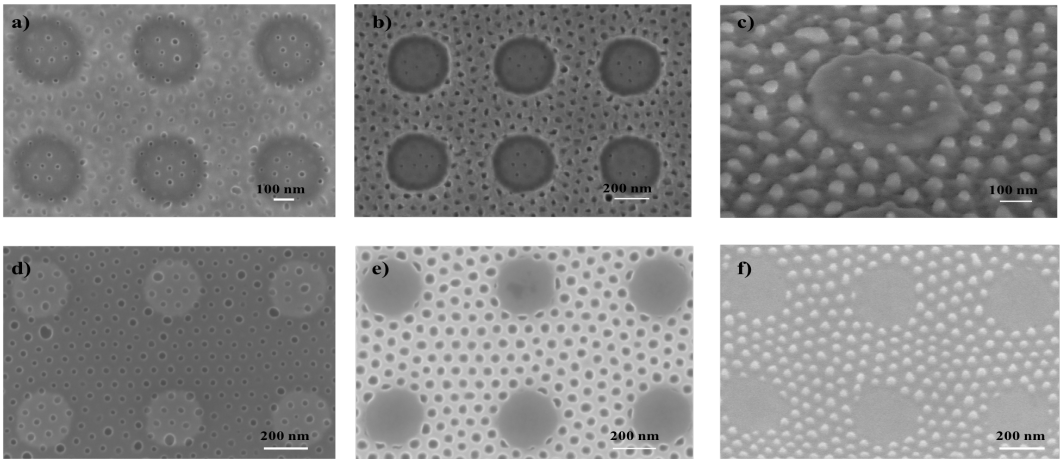

Figure 4.4 *(a) Hexagonally-packed cylinder morphology for holes template, (d) for nanodisk template, (b,e) Dry etching of BCP nanoporous mask into Si, and (c,f) Template stripped Au film.*

4.3 Numerical results

A FDTD solver is used to simulate the interaction of light with the metal NSs. In this section, a numerical analysis of metal NSs, specifically 50 nm thick and 350 nm wide Au disk on Au film as shown in **Figure 4.5 (d)** and same Au disk with 40 nm tall Au nanodomes (**Figure 4.4 (c)**) and 40 nm tall Au nanodomes without Au disk (**Figure 4.4 (f)**) are presented. The results below show the enhancement of the electric field in different regions of the metal NSs.

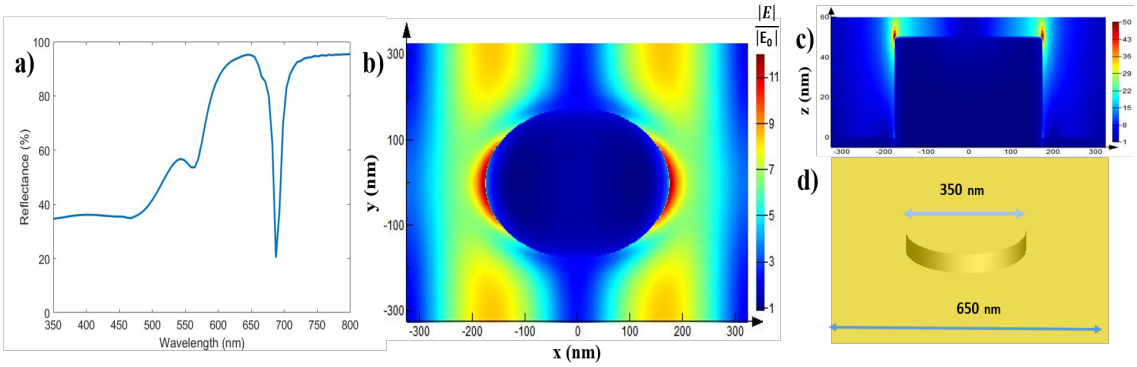

Figure 4.5 *(a) reflectance spectrum, (b) E-field enhancement at plasmon resonance wavelength (687 nm) for horizontal cross-section, (c) for vertical cross-section, (d) for defined geometry for periodic Au disk.*

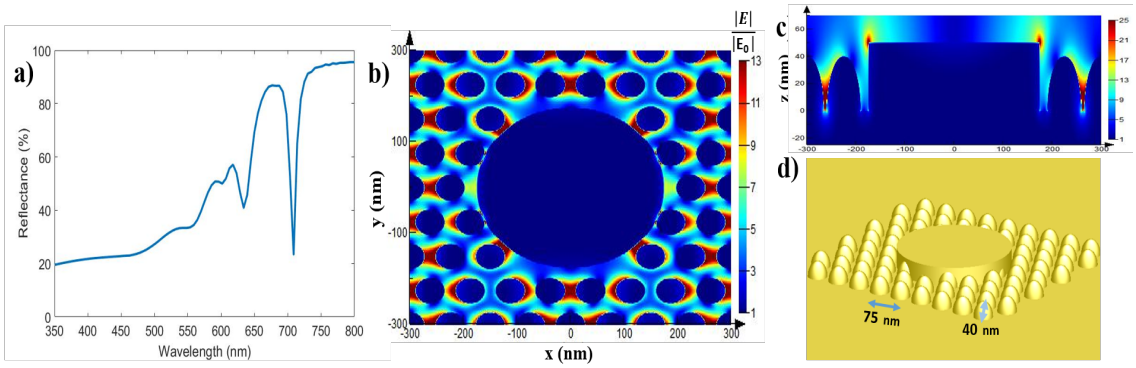

Figure 4.6 *(a) reflectance spectrum, (b) E-field enhancement at plasmon resonance wavelength (708 nm) for horizontal cross-section, (c) for vertical cross-section, (d) for defined geometry for periodic Au disk with BCP Au NSs.*

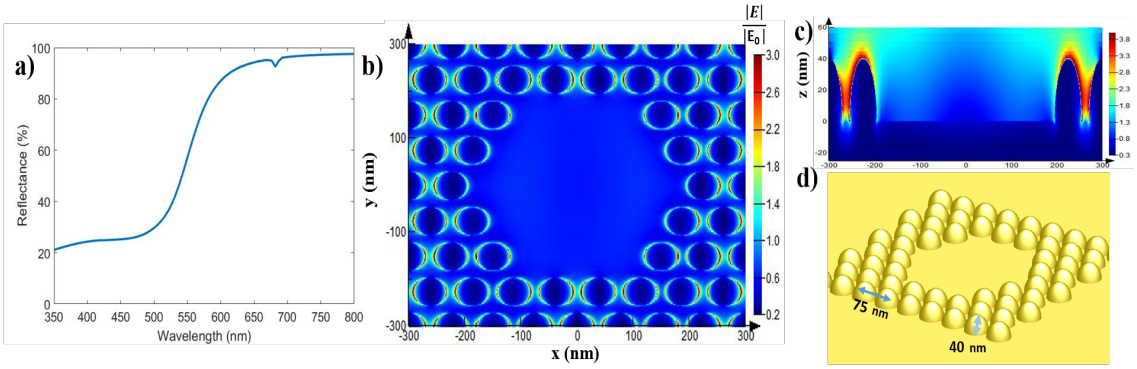

Figure 4.7 *(a) reflectance spectrum, (b) E-field enhancement at plasmon resonance wavelength (681 nm) for horizontal cross-section, (c) for vertical cross-section, (d) for defined geometry for periodic holes with BCP Au NSs.*

Numerical analysis of the realized metal NSs shows the effect of light localization and field enhancement in the vicinity of the metal NSs. The field enhancement in **Figures 4.6** and **4.7** is a consequence of the hybridization of SPR and LSPR. However, the E-field enhancement factor $\frac{|\mathbf{E}|}{|\mathbf{E}_0|}$ for Au disk with Au nanodomes is relatively larger than Au holes with Au nanodomes. The hybridization of SPPs and LSPs can be visualized from **Figure 4.5 (b)**. The strong field localization near the edges of the Au disk is resulted from the LSPR and propagating fundamental SPP mode can be seen around the Au disk. The vertical cross-section of the E-field shown in **Figures 4.6 (c)** and **4.7 (c)** verifies confinement of the E-field hence, strong enhancement in the gaps of the metal NSs.

The theoretical effect of the gap width between BCP metal nanostructres is investigated. Sharp gaps between plasmonic NSs can support gap plasmon modes and are

known to greatly enhance the electric field. The extreme E-field enhancement in 1 nm gaps is demonstrated with the aid of following results.

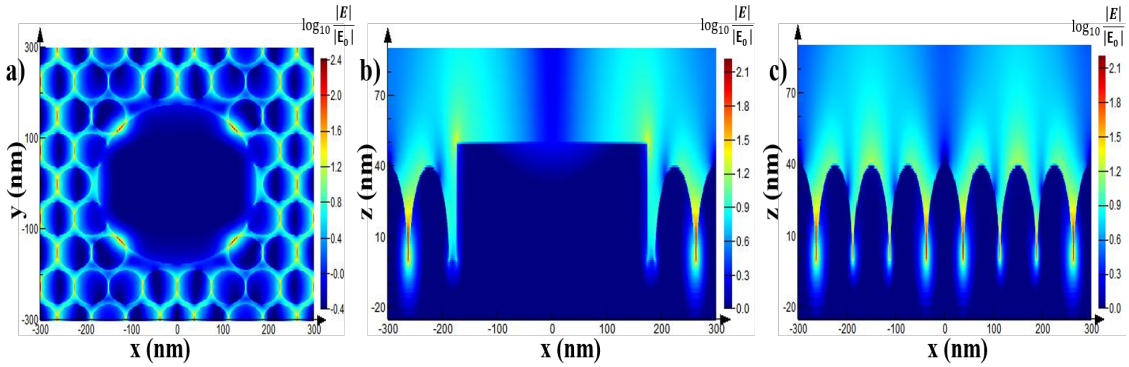

Figure 4.8 *Field enhancement in the geometry defined in* ***figure 4.6 (d)*** *with 1 nm gap between BCP metal NSs.*

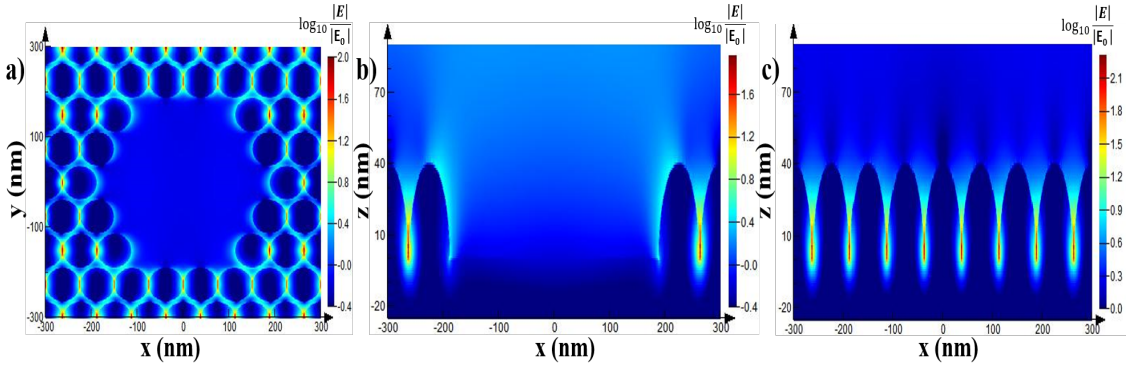

Figure 4.9 *Field enhancement in the geometry defined in* ***figure 4.7 (d)*** *with 1 nm gap between BCP metal NSs.*

Due to extremely large E-field enhancement factor, the color scales for these figures have been changed to log of base-10 for the visualization purposes. The E-field enhancement factor is tens-order greater than the results from **Figures 4.5 - 4.7**.

4.4 Optical Measurements

Once the Au NSs were fabricated, the next step was to determine whether these fabricated structures could support SPP and LSP. As discussed in the **section 2.2.1**, the excitation of SPR is achieved by a grating coupling technique whereas excitation of LSPR can be achieved with direct illumination. The effect of plasmon resonance can be seen as a dip in the spectra in a reflectance measurement.

A commercially available equipment, PerkinElmer LAMBDA 1050 UV/Vis Spectrophotometer, was used for the reflectance measurement. The reflectance was taken at a 8° incident angle in a wavelength range of $350 - 800$ nm. The experimental reflectance results for each geometry are shown with simulation results in **Figures 4.10 - 4.12**. A planar Au thin film is shown as a reference in all figures.

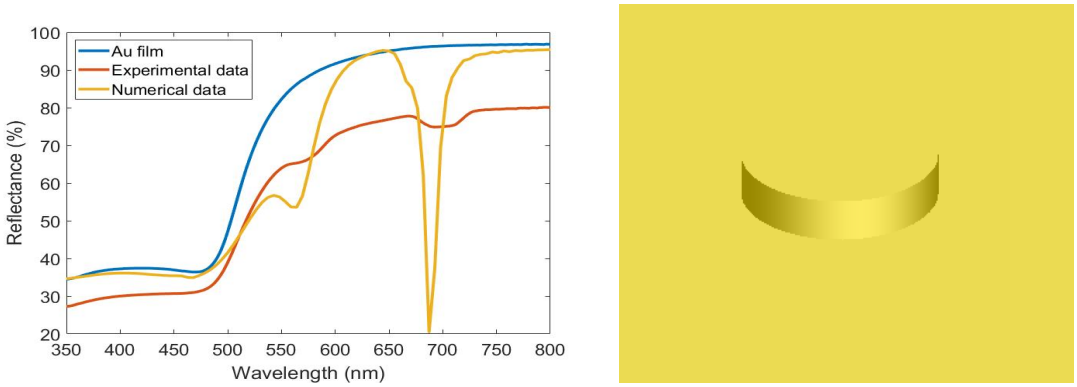

***Figure 4.10 Left**) Reflectance measurement of Au nanodisk on Au film. Comparison with plain Au film (blue curve) and numerical result (yellow curve) from **Figure 4.5 (a)**. Plasmon resonance peak is observed at 687 nm (Numerical) and 700 nm (Experimental). **Right**) Au holes with Au nanodomes.*

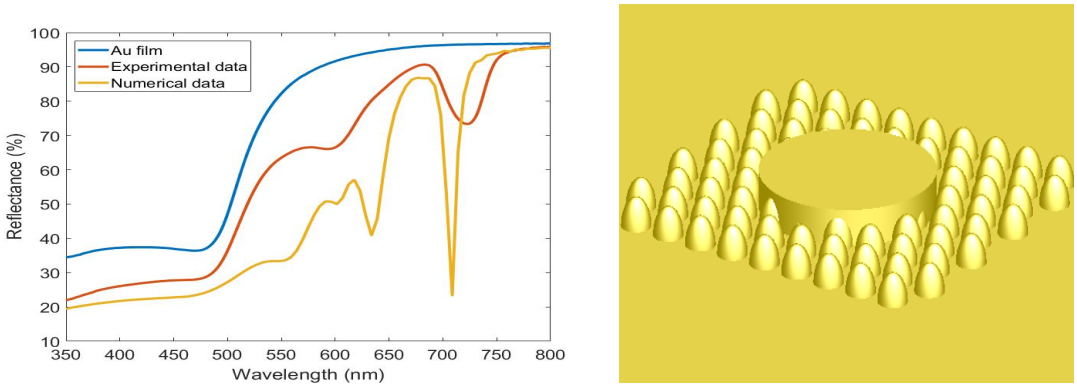

***Figure 4.11 Left**) Reflectance measurement of Au nanodisk with BCP Au NSs on Au film. Comparison with plain Au film (blue curve) and numerical result (yellow curve) from **Figure 4.6 (a)**. Plasmon resonance peak is observed at 708 nm (Numerical) and 722 nm (Experimental). **Right**) Au disk with Au nanodomes*

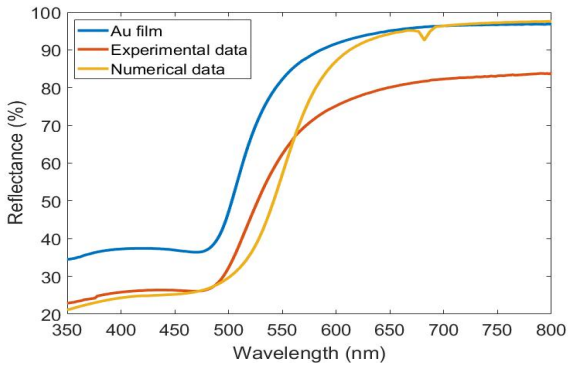

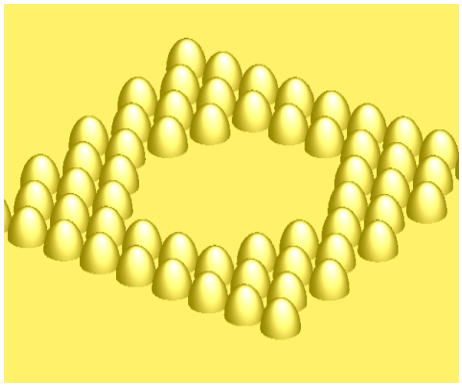

***Figure 4.12 Left**) Reflectance measurement of BCP Au NSs with Au holes. Comparison with plain Au film (blue curve) and numerical result (yellow curve) from **Figure 4.7 (a)**. **Right**) Au holes without Au nanodomes.*

From **Figure 4.10** and **Figure 4.11**, it can be observed that the plasmon resonance wavelength for numerical and experimental results differs slightly. This can be because, for the numerical analysis, the angle of incidence is assumed to be 0°, however, experimentally, the reflectance measurements were taken at an 8° incident angle. The presence of a second plasmon resonance peak observed around 600 nm can be explained by the ± sign in equation (2.2), which means that the wave mode is propagating in both directions (longer wavelength plasmon resonance towards negative direction and shorter wavelength plasmon resonance towards positive direction).

The plasmon resonance peak is quite shallow for experimental results than for the numerical results, which could mean that coupling of the plasmons with the EM wave is not very strong. There is no plasmonic effect seen in **Figure 4.12** for experimental results however, a small dip is seen in the numerical results at 681 nm. It is also evident that the presence of metal NSs on the Au film decreases the reflectance when compared to the reflectance of an unpatterned Au film. This is due to scattering from teh larger structures and plasmon-related absorption.

The presence of plasmon resonance peak for Au disk at 687 nm and for Au disk with Au nanodomes at 708 nm implies that the BCP Au nanodomes shifted the plasmon resonance peak towards higher wavelength. This could mean that the plasmon resonance peak could be tuned to higher or lower wavelength by varying the size and geometry of the BCP NSs.

5. CONCLUSIONS

BCP lithography provides a promising alternative for nanofabrication in the sub-wavelength regime. The feature sizes and pattern densities that can be realized with BCP lithography range from under tens of nms to a few hundred nms. These types of dense, nanometer-scale patterns are currently difficult or time-consuming to obtain using other nanolithography techniques. A comparision between different lithography techniques and the obtained feature sizes can be seen in **Figure 5.1**.

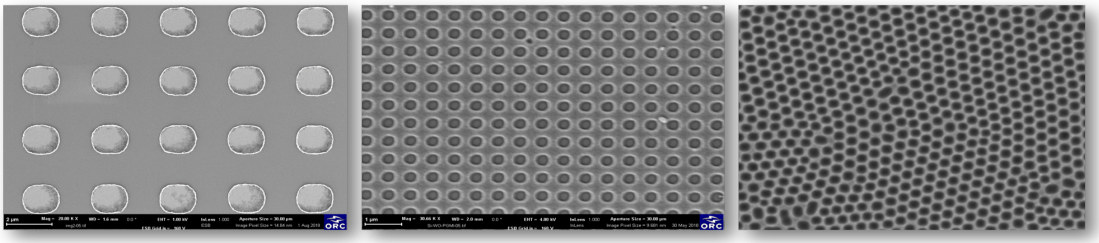

Optical lithography : Chromium cylinders
Size = 2 microns
Periodicity = 5 microns

Nano-imprint lithography : Holes in Silicon
Hole size = 350 nm
Periodicity = 650 nm

BCP lithography : Holes in Silicon
Hole size = <50 nm
Periodicity = 75 nm

Figure 5.1 *Feature sizes from different lithography techniques.*

The use of BCP lithography and Au template stripping to produce metallic sub-wavelength NSs has been demonstrated. The excitation of SPR is achieved using nano-scale diffracting structures fabricated by NIL. Sub-wavelength metallic NSs were also observed to induce LSPR. However, the coupling of LSPR in the experimental work was not as strong as was expected. This could be due to the lack of control over pattern formation via self-assembly in BCP lithography, resulting in irregular periodicity and size-variation of the BCP metal NSs.

BCP lithography is an active field of research for sub-wavelength nanofabrication and possibly a strong candidate for next-generation lithography. With substantial ongoing research in this field, a better control over the self-assembly process is certainly to be expected. As a continuation in the direction of this thesis work, testing with different BCPs and polymer sizes could be an option for achieving efficient, plasmon-mediated visible light absorption in sub-wavelength patterned Au thin films.

BIBLIOGRAPHY

[1] Maier, S., 2007. Plasmonics: Fundamentals and Applications. (pp. 3-87). 1st ed. 223 Spring Street, New York, NY 10013, USA: Springer-Verlag New York, LLC.

[2] O., Takayama, A.A.,Bogdanov, and A.V., Lavrinenko, 2017. Photonic surface waves on metamaterial interfaces. Journal of Physics: Condensed Matter, 29, 463001. Available at: http://stacks.iop.org/0953-8984/29/i=46/a=463001

[3] Tapan K Sarkar, Mohammad N Abdallah, Magdalena Salazar-Palma, Walid M Dyab, 2017. Surface Plasmons-Polaritons, Surface Waves, and Zenneck Waves: Clarification of the terms and a description of the concepts and their evolution. IEEE Antennas and Propagation Magazine, 59-3, 77-93. Available at: https://ieeexplore.ieee.org/stamp/stamp.jsp?arnumber=7915676

[4] Rasappa, S. 2013. Block copolymer self-assembly based device structures. PhD Thesis, University College Cork, Cork, Ireland. Available at: https://cora.ucc.ie/handle/10468/1237

[5] Gu, Xiaodan, "Self-Assembly of Block Copolymers by Solvent Vapor Annealing, Mechanism and Lithographic Applications" (2014). Doctoral Dissertations. 7. Available at: https://scholarworks.umass.edu/dissertations_2/7

[6] Hulkkonen, H., Salminen, T., and Niemi, T. Block Copolymer Patterning for Creating Porous Si Thin Films with Tunable Refractive Indices. ACS Applied Materials & Interfaces 2017 9 (37), 31260-31265. DOI: 10.1021/acsami.6b16110

[7] Viheriälä, J., 2010. Nanoimprint Lithography - A Next Generation Patterning Method for Nanophotonics. (pp. 8-13). Ph.D. Tampere, Finland: Tampere University of Technology.

[8] Elsherbeni, Atef Z. Demir, Veysel. (2016). Finite-Difference Time-Domain Method for Electromagnetics with MATLAB® Simulations (2nd Edition). (pp. 1-32). Institution of Engineering and Technology. Available at: https://app.knovel.com/hotlink/toc/id:kpFDTDMEM7/finite-difference-time/finite-difference-time

[9] Christopher Siefe. (2014).*Surface plasmon*, image, viewed on November 2018. Available at: https://undergrad.research.ucsb.edu/2014/04/surface-plasmons-awesome-group/

[10] Alice Huang. (2015). *Comparing LSPR and SPR for Diagnostics - LamdaGen.* [online video], viewed November 2018. Available at: https://www.youtube.com/watch?v=QLT1vrnJXWI&t=103s

[11] Briliant Adhi Prabowo, Agnes Purwidyantri, and Kou-Chen Liu. Surface Plasmon Resonance Optical Sensor: A Review on Light Source Technology. Biosensors 2018, 8(3), 80; https://doi.org/10.3390/bios8030080